JOURNAL OF AIRCRAFT
Vol. 44, No. 5, September–October 2007

Navier–Stokes Analysis of Airfoils with Gurney Flap

Manish K. Singh,* K. Dhanalakshmi,* and S. K. Chakrabartty*
National Aerospace Laboratories, Bangalore 560 017, India

DOI: 10.2514/1.27285

Two-dimensional steady-state Navier–Stokes computations were performed to determine the effect of Gurney flap on NACA 0011 and NACA 4412 airfoils. Gurney flap sizes selected for the study range from 0.5 to 4% of the airfoil chord. A compressible Navier–Stokes solver with Baldwin–Lomax turbulence model, JUMBO2D, is used to predict the flowfield around the airfoils. Computed results have been compared with available experimental and computational data. There is good correlation observed between computed and experimental data. Addition of Gurney flap increases the lift coefficient but with drag penalty, which is not very significant for smaller Gurney flap. The effect of Gurney flap on aerodynamic efficiency has also been studied. Nose-down pitching moment also increases with Gurney flap height. Flowfield structure near the trailing edge shows very good resemblance with Liebeck's hypothesis that provides the possible explanation for the increased aerodynamic performance.

I. Introduction

HIGH lift systems play a major role in performance and economic success of commercial, transport and military aircraft. An efficient high lift system offers many advantages like lower takeoff and landing speed, greater payload capacity for given wing, longer range for given gross weight, and higher maneuverability. High lift systems are desired to maintain low drag at takeoff so as to attain cruise speed faster and high drag at approach. High lift systems are often quite complex, consisting of many elements and multi bar linkages. Therefore there is need to have simpler high lift systems that are cheaper in terms of manufacturing and maintenance cost. One such candidate is Gurney flap.

Gurney flap is a small flat plate, in the order of 1–2% of airfoil chord in height, fitted to the pressure side of airfoil at the trailing edge and perpendicular to the chord line. Don Gurney first used this trailing-edge device in racing cars to increase the downward force during high velocity cornering [1]. Gurney noticed a reduction in drag, which he measured by comparing the corner and straightaway speeds with and without the flap. It was also found that increasing the flap height beyond 2% of chord led to an increase in the downward force but at the cost of significant drag penalty.

Liebeck [1] conducted wind tunnel tests on the Newman airfoil with 1.25% chord Gurney flap. He found that lift increases for a given angle of attack, and the drag reduces for a given lift. A tufted probe at the trailing edge indicated significant turning of flow over the backside of the Gurney flap. He hypothesized that Gurney flap causes flow to turn towards the flap near the trailing edge by introducing two counterrotating vortices aft of the Gurney flap (Fig. 1).

Myose et al. [2] conducted low-speed wind tunnel tests on NACA 0011 airfoil with Gurney flap heights ranging from 1 to 4% of the chord. They noticed that Gurney flap increases the upper surface suction and lower surface pressure, thereby resulting in lift increment. They also reported an increase in nose-down pitching moment due to Gurney flap. The wake velocity profiles plotted by them indicate downward turning of the flow behind the airfoil due to presence of Gurney flap. They concluded that Gurney flap works by increasing the effective camber of airfoil.

Jang et al. [3] used an incompressible Navier–Stokes code to compute flowfield about NACA 4412 airfoil with Gurney flap heights ranging from 0.5 to 3% of chord. Computations predicted increase in lift coefficient and nose-down pitching moment. Computations also show that at moderate angle of attack, Gurney flap causes separation points on suction surface to shift aft as compared to clean airfoil. They noticed an increment in loading along entire length of the airfoil when Gurney flap is used.

Storms and Jang [4], who conducted an experimental study on NACA 4412 airfoil with Gurney flap, reported similar trends. However, they observed that though there is good correlation between experiment and computational lift coefficient obtained by Jang et al. [3] for clean airfoil, the lift increment caused by Gurney flap was underpredicted.

The primary objective of the present work is to study the flow past NACA 0011 and NACA 4412 airfoils with Gurney flaps of different heights using the compressible Reynolds-averaged Navier–Stokes analysis code JUMBO2D and to compare these results against available experimental and computational results.

II. Basic Equations

The 2-D, unsteady Navier–Stokes equations, neglecting body forces and heat sources, can be written in the integral form as

$$\frac{\partial}{\partial t}\iiint_V \boldsymbol{W}\,\mathrm{d}V + \iint_S \bar{\bar{F}}_E \cdot \boldsymbol{n}\,\mathrm{d}S + \iint_S \bar{\bar{F}}_V \cdot \boldsymbol{n}\,\mathrm{d}S = 0 \tag{1}$$

where

$$\boldsymbol{W} = \begin{bmatrix} \rho \\ \rho u \\ \rho v \\ \rho E \end{bmatrix}, \qquad \bar{\bar{F}}_E = \begin{bmatrix} \rho \boldsymbol{q} \\ \rho u \boldsymbol{q} + p \mathbf{e}_x \\ \rho v \boldsymbol{q} + p \mathbf{e}_y \\ \rho H \boldsymbol{q} \end{bmatrix}$$

$$\bar{\bar{F}}_V = \begin{bmatrix} 0 \\ \bar{\bar{\boldsymbol{\tau}}} \cdot \boldsymbol{e}_x \\ \bar{\bar{\boldsymbol{\tau}}} \cdot \boldsymbol{e}_y \\ \bar{\bar{\boldsymbol{\tau}}} \cdot \boldsymbol{q} - \boldsymbol{Q} \end{bmatrix} \qquad \boldsymbol{q} = u\boldsymbol{e}_x + v\boldsymbol{e}_y, \qquad H = E + p/\rho$$

$$E = \frac{RT}{\gamma - 1} + \frac{1}{2}(u^2 + v^2) \qquad \bar{\bar{\boldsymbol{\tau}}} = \begin{bmatrix} \sigma_x & \boldsymbol{\tau} xy \\ \boldsymbol{\tau} yx & \sigma_y \end{bmatrix}$$

$$\sigma_x = -\lambda\left(\frac{\partial u}{\partial x} + \frac{\partial v}{\partial y}\right) - 2\mu\frac{\partial u}{\partial x} \qquad \sigma_y = -\lambda\left(\frac{\partial u}{\partial x} + \frac{\partial v}{\partial y}\right) - 2\mu\frac{\partial v}{\partial y}$$

$$\boldsymbol{\tau}_{xy} = -\mu\left(\frac{\partial u}{\partial y} + \frac{\partial v}{\partial x}\right) = \boldsymbol{\tau}_{yx} \qquad \boldsymbol{Q} = k\nabla T = k\left(\frac{\partial T}{\partial x}\boldsymbol{e}_{\boldsymbol{x}} + \frac{\partial T}{\partial y}\boldsymbol{e}_{\boldsymbol{y}}\right)$$

Here V is a control volume with surface S and normal $\boldsymbol{n}$. Let ρ, (u, v), p, T, E, H, γ be the density, Cartesian velocity components, pressure, temperature, total internal energy, total enthalpy, and ratio of specific heats, respectively. $\boldsymbol{e}_x$, $\boldsymbol{e}_y$ are the unit vectors in the

---

Received 18 August 2006; revision received 18 October 2006; accepted for publication 29 November 2006.

*Computational and Theoretical Fluid Dynamics Division, Post Box 1779.

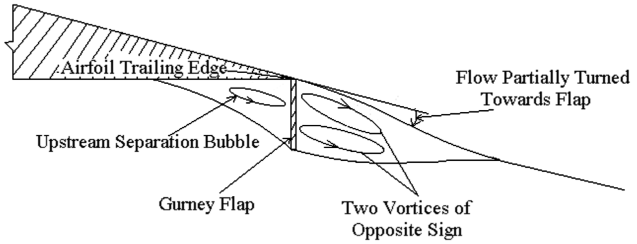

Fig. 1 Hypothesized trailing-edge flowfield for an airfoil with Gurney flap [1].

Cartesian coordinate system, and k is coefficient of thermal conductivity.

$\boldsymbol{W}$ represents the vector of conserved variables, $\bar{\bar{F}}_E$ represents the Euler fluxes, $\bar{\bar{F}}_V$ represents the viscous fluxes, $\boldsymbol{Q}$ is the heat flux, and $\bar{\bar{\tau}}$ is the stress tensor. μ and λ are the first and second coefficients of viscosity, and $\lambda = -2/3\mu$, using Stokes' hypothesis. μ and T are related by Sutherland's law. The coefficient of thermal conductivity has been evaluated using constant Prandtl number assumption and it is assumed to be unity. The preceding set of equations is complete with the perfect gas relation $p = \rho RT$, where R is the gas constant.

III. Boundary Conditions

The different types of boundaries encountered are solid wall, internal cuts, and far-field. One extra layer of image cells, surrounding the computational domain, is necessary to implement the boundary conditions. Implementation of the surface boundary conditions involves an image principle. According to that a fictitious cell is placed inside the body to obtain first order derivatives at the centers of the cells surrounding a surface control point for computing viscous fluxes. At the solid wall boundary, no-slip condition is applied, by setting the velocity components u and v equal to zero. The adiabatic wall condition is applied by setting the normal derivative of the temperature equal to zero.

Two different types of internal cut boundaries arise, and their treatment varies slightly. The first type of internal cut is required in the physical domain to make the computational domain simply connected. For this type of cut, periodic boundary conditions are implemented by forming image cells on both edges of the computational domain, where proper correspondence between the grid cells and the image cells is taken care of by specifying the image block, face, and the orientation of the segment. The second type of cut arises at the interblock boundaries when the computational domain is split into a number of computational blocks, and interblock continuity is enforced here by connecting cells of one face segment of the computational block to the corresponding face segment of the image block with proper orientation. Thus, whereas there are three overlapping grid lines for the first type of cut, there are only two such lines for the second type of cut.

The treatment of the far-field boundary is based on the Riemann invariants for 1-D flow normal to the boundary. The Riemann invariants of incoming and outgoing characteristics are calculated using freestream conditions and by extrapolation from the interior of the field, respectively. Boundary values for the normal velocity component and speed of sound are computed by adding and subtracting these invariants. At an inflow boundary, the tangential velocity components and the entropy are prescribed from their freestream values, whereas at an outflow boundary these values are extrapolated from the interior. The details of boundary conditions and their implementation are available in [5].

IV. Methodology

The JUMBO2D computer code solves the 2-D Reynolds-averaged Navier–Stokes (RANS) equations using a vertex-based finite volume space discretization and five-stage Runge–Kutta time integration. The algebraic turbulence model used is the one described in [6] as model 2, which is a modified form of the Baldwin–Lomax model [7]. Details of the governing equations, boundary conditions, finite volume formulation, time integration, and the turbulence model used are available in [5,6,8,9]. Local time stepping, enthalpy damping, and implicit residual smoothing are used for convergence acceleration [10].

The code is independent of the grid topology used, and the only necessary input is grid data. The computational domain can be subdivided into smaller subdomains/blocks and computation can be carried out blockwise to reduce the current memory requirement and to facilitate parallel computation. The type of boundary condition to be applied at each segment of a face of a particular block can be specified through input data. These make the code very flexible and allow the same code to solve a variety of flow problems. A novel space discretization scheme is used here for the viscous terms, which facilitates computation of full Navier–Stokes equations with about the same numerical effort as for the thin layer type of approximation [8].

The finite volume discretization amounts to central differencing and thus requires the addition of explicit dissipation terms for stability in supersonic regions. The blended second- and fourth-order artificial dissipation, defined in [9], damps the high-frequency oscillations and prevents odd–even point decoupling for inviscid flows and introduces appropriate dissipation near the shock to allow an entropy condition to be satisfied. It thus guarantees the uniqueness of weak solutions. For viscous flows, although the dissipative properties are present in the equations, these may not be sufficient for stability due to nonlinear effects especially in the case of highly stretched meshes required to resolve the boundary layer. For accurate results, the numerical dissipation should not overwhelm the natural dissipation. The turbulent eddy viscosity μ_t, calculated by an algebraic turbulence model, is added to its laminar counterpart μ_l to get the effective viscosity μ. The coefficient of thermal conductivity k can be calculated as

$$k = \mu C_p \tag{2}$$

where C_p is specific heat at constant pressure.

V. Geometrical Modeling and Grid Generation

NACA 0011 and NACA 4412 airfoils are considered for this study. Gurney flap sizes of 1, 2, and 4% chord length have been chosen for NACA 0011 airfoil and 0.5, 1, 1.5, and 2% of chord length for NACA 4412 airfoil. These particular Gurney flap sizes are considered to make comparison with available experimental and computational results. Gurney flaps are located at the trailing edge on the pressure side of the airfoil perpendicular to the chord and the thickness of the flap is one grid cell width. Gurney flaps with zero thickness (i.e., coinciding with a grid line) were also tried but the solutions did not vary significantly from the present results.

Commercially available grid generation software Gridgen† has been used to generate structured grids. Hyperbolic tangent distribution function is used to determine the point distribution on the boundaries. Transfinite interpolation is employed to determine interior point distribution and elliptic PDE method has been used to smooth and improve grid quality. A single block C-type structured grid has been generated for computing the flowfield for clean airfoils. A three-block (Fig. 2a) structured grid, with one block below the wake centerline, another block around the airfoil, and the third one above the wake centerline, is employed to compute the flowfield for airfoils with Gurney flaps. A typical grid used for NACA 4412 airfoil with Gurney flap is shown in Fig. 2b and its closeup view in the vicinity of the airfoil is shown in Fig. 2c. The dimensions of grids are listed in Tables 1 and 2. The upstream, downstream, top, and bottom boundaries are located at 16 chord lengths away. The first grid point above the airfoil surface is such that the law of the wall coordinate $y+$ is of the order of 5. Various grid dimensions and far-field distances

---

†Details available online at http://www.pointwise.com [cited 22 January 2007].

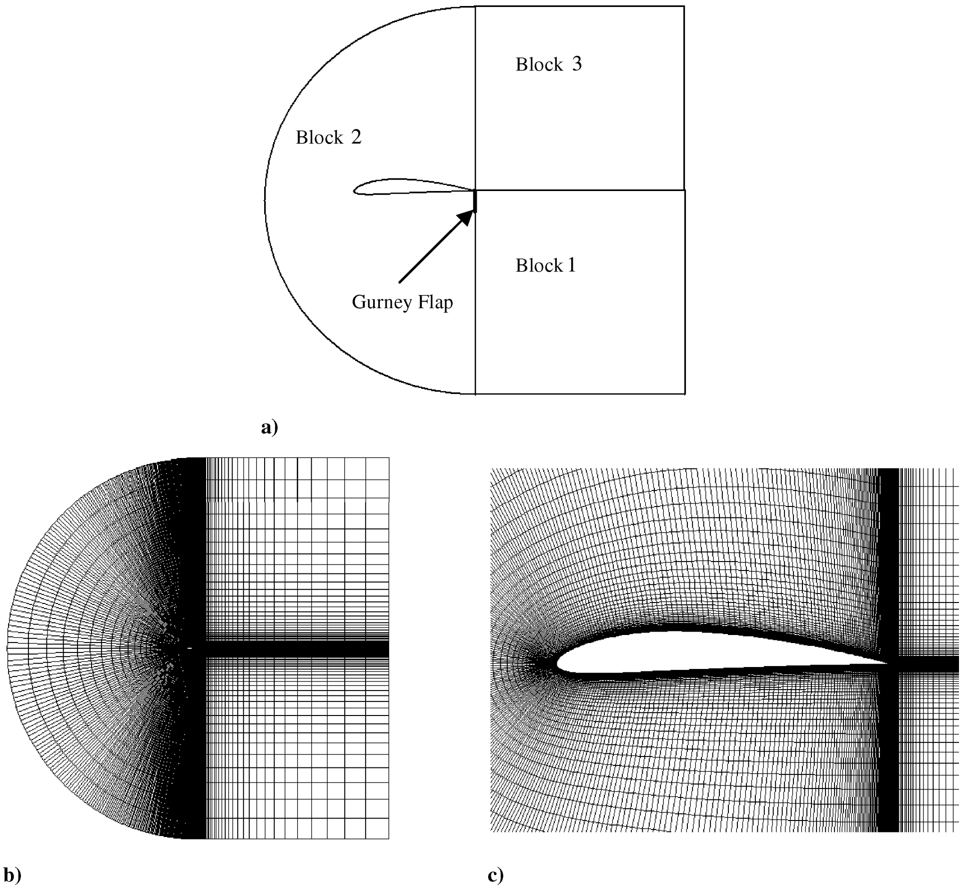

a)

b) c)

Fig. 2 a) Block arrangement for computation of flow past airfoil with Gurney flap. b) Grid used in computation for NACA 4412 airfoil with Gurney flap. c) Closeup of grid in the vicinity of airfoil.

were tried and the present grids were found to be optimum in capturing the complex flow physics of the Gurney flap. For the application of turbulence model, in the vicinity of Gurney flap, normal distance is taken as the minimum of the two distances measured from the airfoil surface and the Gurney flap.

VI. Results and Discussion

All the computations in this study for NACA 0011 airfoil are performed for freestream Mach number of 0.14 and chord Reynolds number of 2.2×10^6 and those for NACA 4412 airfoil are carried out for Mach number 0.2 and chord Reynolds number of 2.0×10^6. These flow parameters for computations were chosen to make comparison with available experimental results. The JUMBO2D solver code used in the present analysis has been extensively validated and applied to a variety of flow problems [6,11,12].

Table 1 Grid dimension for NACA 0011

	Block number			Points on Gurney flap
	1	2	3	
Clean airfoil	347 × 62	——	——	——
1.0% Gurney	45 × 62	258 × 62	45 × 62	20
2.0% Gurney	45 × 91	258 × 91	45 × 91	28
4.0% Gurney	70 × 91	358 × 91	70 × 91	48

Table 2 Grid dimension for NACA 4412

	Block number			Points on Gurney flap
	1	2	3	
Clean airfoil	497 × 62	——	——	——
0.5% Gurney	70 × 73	358 × 73	70 × 73	30
1.0% Gurney	70 × 91	358 × 91	70 × 91	40
1.5% Gurney	70 × 91	358 × 91	70 × 91	40
2.0% Gurney	70 × 91	358 × 91	70 × 91	50

The computed aerodynamic data for NACA 0011 and NACA 4412 airfoils are presented in Figs. 3 and 4, respectively. Figures 3a and 4a show the variation of lift coefficient C_L with Gurney flap height and also the comparison with available experimental data. It is evident from these figures that there is significant nonlinear increment in lift with Gurney flap height. For example, lift increment due to Gurney flap of 1% chord height with respect to the clean airfoil is higher than that obtained by changing Gurney flap height from 1% chord to 2% chord in both airfoils. Computational results predicted stall angle higher by 2–3 deg as compared to the experimental results. Under prestall conditions it is observed that there is good agreement between computational and experimental data for NACA 0011 airfoil with and without Gurney flap, except in the case of 4% chord Gurney flap where computations seem to underpredict the lift coefficient. It is also noted that computations are overpredicting the lift compared to experiment for NACA 4412 airfoil with and without Gurney and the difference between computation and experiment is increasing with angle of attack. These differences are probably due to the fact that flow is increasingly becoming unsteady at higher angle of attack and particularly beyond stall whereas computations assume flow to be steady.

The effect of Gurney flap on drag and comparison with experimental results is presented in Figs. 3b and 4b. For low angles of attack, it is observed that computational results are in good agreement with experimental results except in case of NACA 0011 airfoil with 4% chord Gurney flap, where computational results underpredicted the drag. Gurney flap increases the drag coefficient C_D for all prestall incidences. Substantial drag increment is observed when Gurney flap height is increased to 4% chord.

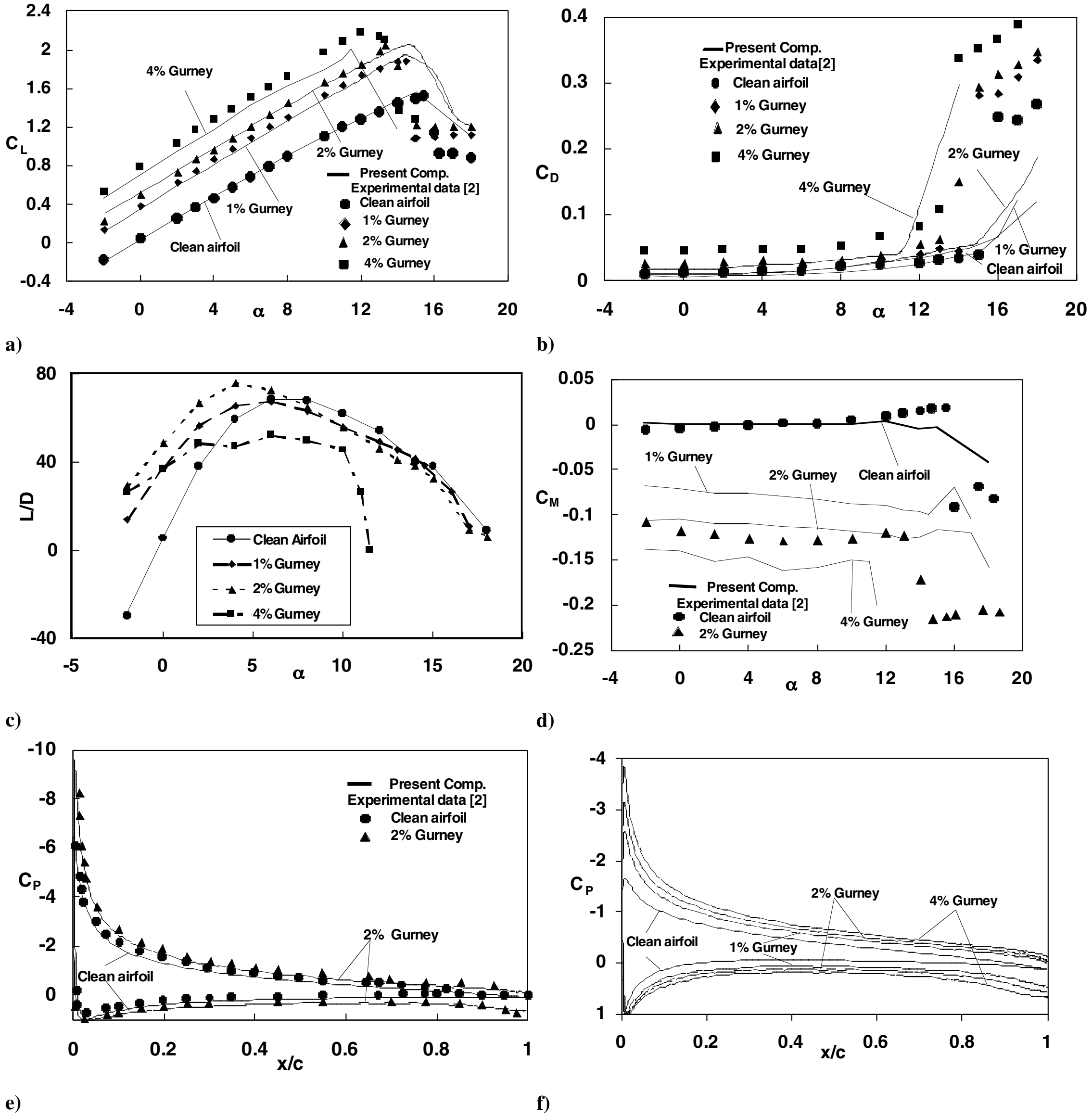

Fig. 3 NACA 0011 airfoil. a) Comparison of lift coefficient between computations and experiment for various Gurney flap sizes. b) Comparison of drag coefficient between computations and experiment for various Gurney flap sizes. c) Comparison of airfoil efficiency for different flap sizes. d) Comparison of quarter-chord pitching moment for various Gurney flap sizes. e) Comparison of pressure coefficients between computations and experiments at $\alpha = 10$ deg. f) Pressure distribution for different Gurney flap sizes at $\alpha = 4$ deg.

The effect of Gurney flap on the aerodynamic efficiency has been demonstrated by plotting lift to drag ratio L/D against angle of attack α and shown in Figs. 3c and 4c for the two airfoils considered. For NACA 0011 airfoil, efficiency increases with flap height up to 2% of the chord but it decreases for the flap height of 4% chord. Opposite behavior has been observed for NACA 4412 airfoil, where the efficiency reduces by use of the Gurney flap. Giguere et al. [13] observed that efficiency increases by use of the Gurney flap up to 2% of the chord for the airfoils, LA 203A-UL and Gottingen 797, which is similar to what has been observed for NACA 0011 airfoil in present study.

Figures 3d and 4d show how Gurney flap affects the pitching moment coefficient C_M (about quarter-chord point) of airfoil for given angle of attack. Similar to the lift coefficient, nose-down pitching moment increases but the increment becomes less with increasing Gurney flap height. Computed values of the moment coefficients and particularly the slope compare well with those of the experimental results under the prestall conditions.

Comparisons of pressure coefficient C_P distribution with experiments [2,4] are presented in Figs. 3e and 4e. They show good agreement with experiments. It is evident from airfoil pressure distributions (Figs. 3f and 4f) that the presence of Gurney flap increases the pressure difference between the upper and lower surfaces of the airfoil, especially near leading and trailing edge. This leads to increase in lift coefficient. An increase in Gurney flap height also produces a similar effect. It can be noted that there is adverse pressure gradient caused by Gurney flap near the trailing edge on the pressure side of airfoil and upstream of Gurney flap.

The effect of Gurney flap on the location of separation point on the airfoil upper surface for moderate angles of incidence is presented in Figs. 5a and 5b. It is observed that addition of Gurney flap shifts the separation point downstream compared to clean airfoil. Larger flap pushes the separation point further aft. But beyond a certain limit, larger flap causes no further aft ward shift in separation point. In fact, for NACA 0011 airfoil with 4% chord Gurney flap, the separation point shifts upstream with respect to that of 1% chord Gurney. Similarly, for NACA 4412 airfoil with 2% chord Gurney flap, the separation point moves upstream compared to 1% chord Gurney. It is also observed that separation occurs early on a clean airfoil than on an airfoil with Gurney flap with respect to the angle of attack.

Variation of lift coefficient and the distribution of pressure coefficient are shown in Figs. 6a and 6b, respectively, with comparison between experimental [4], incompressible computation [3], and present computation for NACA 4412 airfoil with 1% chord

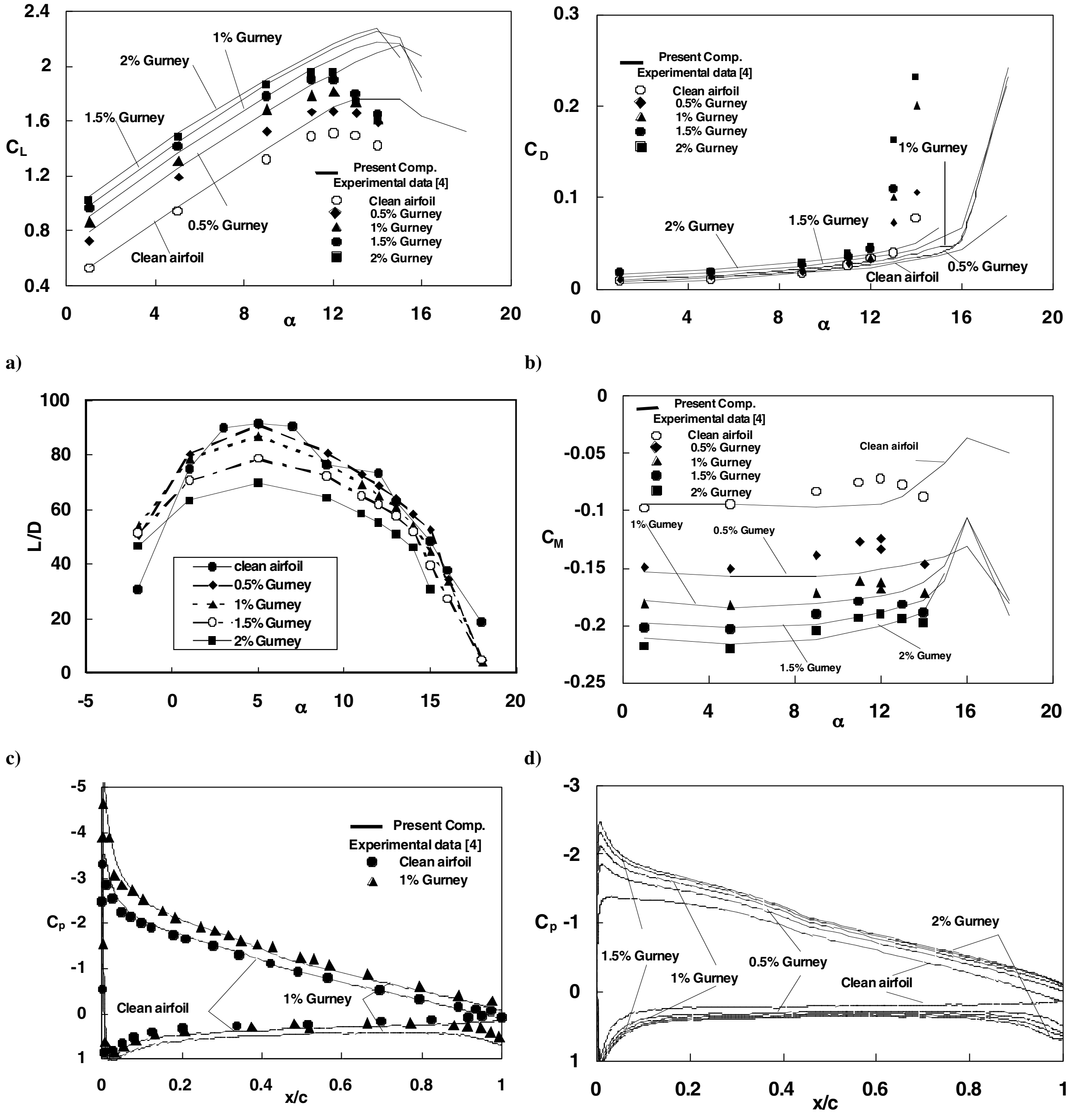

a)

b)

c)

d)

e)

f)

Fig. 4 NACA 4412 airfoil. a) Comparison of lift coefficient between computations and experiment for various Gurney flap sizes. b) Comparison of drag coefficient between computations and experiment for various Gurney flap sizes. c) Comparison of airfoil efficiency for different flap sizes. d) Comparison of quarter-chord pitching moment for various Gurney flap sizes. e) Comparison of pressure coefficients between computations and experiments at $\alpha = 9$ deg. f) Pressure distribution for different Gurney flap sizes at $\alpha = 5$ deg.

Gurney flap. The present computation overpredicts the lift coefficient but is closer to the experimental data than those obtained in [3] using incompressible flow computation. Present C_P distribution lies between those obtained by experiment and incompressible flow results on the upper surface of the airfoil, whereas on the lower surface there is no significant difference between those obtained by compressible and incompressible computation.

Mach contours and streamlines in the vicinity of the trailing edge are shown in Figs. 7 and 8 for the two airfoils considered with 2% chord Gurney flap. Three vortices, one upstream of Gurney flap and two counterrotating vortices downstream of the flap, can be seen as hypothesized by Liebeck [1] and shown in Fig. 1. However, incompressible RANS computation [3] could not capture counterrotating vortices aft of the Gurney flap. It is observed from the flowfield comparison that Gurney flap causes flow to turn downward beyond the flap. This is in agreement with Liebeck's [1] wind tunnel test, in which a tufted probe indicated significant turning of the flow downstream of the flap. The adverse pressure gradients observed upstream of the flap on the lower surface, shown in Figs. 3e and 4e, may be attributed to the formation of recirculating/cove vortices.

VII. Conclusions

Compressible flow past NACA 0011 and NACA 4412 airfoils with Gurney flap has been studied in detail using a RANS code (JUMBO2D) with algebraic turbulence model. Computational results are found to agree reasonably well with available experimental data. Use of Gurney flap increases lift coefficient and nose-down pitching moment compared to those obtained for clean airfoil; however, these increments are nonlinear with respect to flap height. There is an increase in drag for all prestall incidences, but this increment is quite substantial for 4% chord Gurney flap. The aerodynamic efficiency shows improvement in the case of symmetric NACA 0011 airfoil with Gurney flap for low angles of incidence. Such a trend is not observed in the case of cambered NACA 4412 airfoil. The presence of Gurney flap increases the upper surface suction and the lower surface pressure causing increment in loading

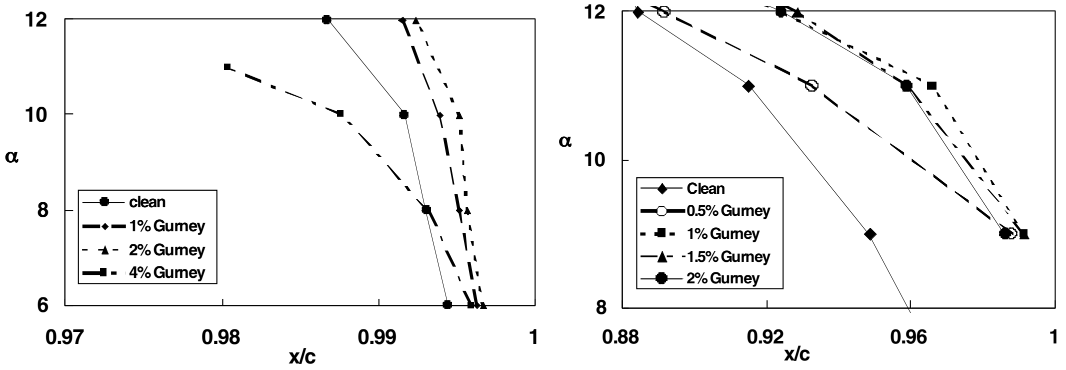

a) b)

Fig. 5 Comparison of flow separation locations on suction side of airfoils for various Gurney flap sizes: a) NACA 0011 airfoil, b) NACA 4412 airfoil.

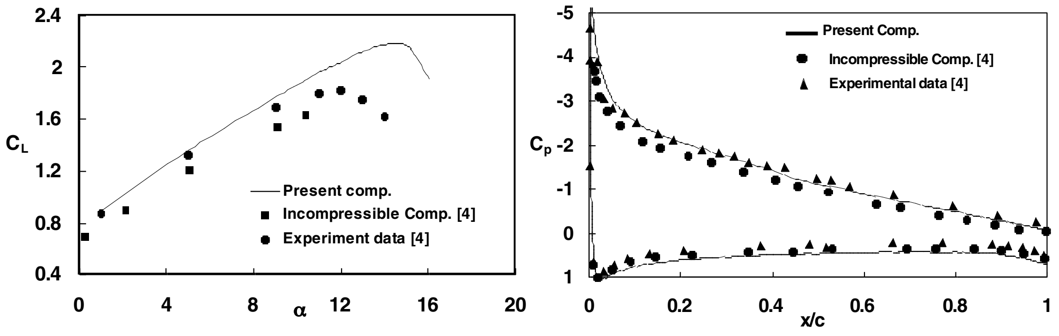

a) b)

Fig. 6 NACA 4412 airfoil with 1% chord Gurney. a) Comparison of experimental and computed lift coefficient. b) Comparison of pressure distribution at $\alpha = 9$ deg.

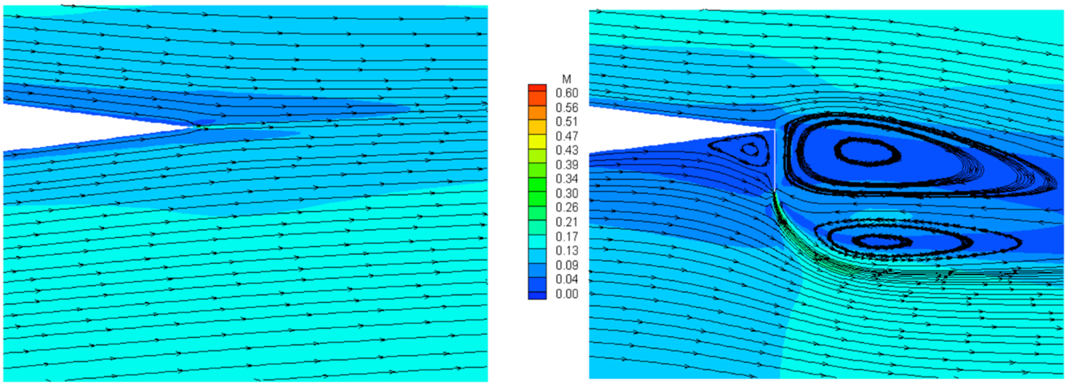

a) b)

Fig. 7 a) Mach contour and stream lines around trailing edge of clean NACA 0011 airfoil at $\alpha = 4$ deg. b) Mach contour and stream lines around trailing edge of NACA 0011 airfoil with 2% chord Gurney flap at $\alpha = 4$ deg.

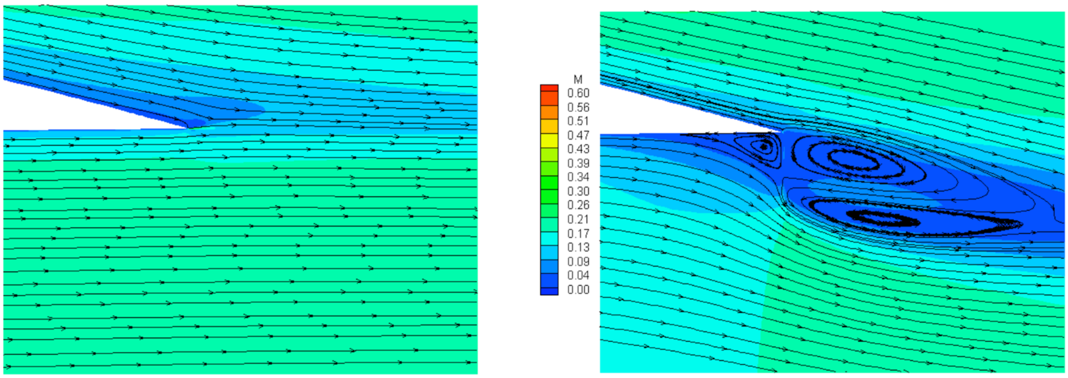

a) b)

Fig. 8 a) Mach contour and stream lines around trailing edge of clean NACA 4412 airfoil at $\alpha = 5$ deg. b) Mach contour and stream lines around trailing edge of NACA 4412 airfoil with 2% chord Gurney flap at $\alpha = 5$ deg.

along entire length of airfoil, noticeably near the trailing edge. Flowfield comparison shows that addition of Gurney flap causes downward turning of the flow behind the Gurney flap.

References

[1] Liebeck, R. H., "Design of Subsonic Airfoils for High Lift," *Journal of Aircraft*, Vol. 15, No. 9, 1978, pp. 547–561.

[2] Myose, R., Heron, I., and Papadakis, M., "The Effect of Gurney Flaps on a NACA 0011 Airfoil," AIAA Paper 96-0059, Jan. 1996.

[3] Jang, C. S., Ross, J. C., and Cummings, R. M., "Computational Evaluation of an Airfoil with a Gurney Flap," AIAA Paper 92-2708, June 1992.

[4] Storms, B. L., and Jang, C. S., "Lift Enhancement of an Airfoil Using a Gurney Flap and Vortex Generators," *Journal of Aircraft*, Vol. 31, No. 3, 1994, pp. 542–547.

[5] Niyogi, P., Chakrabartty, S. K., and Laha, M. K., *Introduction to Computational Fluid Dynamics*, Pearson Education, New Delhi, India, 2005.

[6] Chakrabartty, S. K., and Dhanalakshmi, K., "Computation of Transonic Flow with Shock-Induced Separation Using Algebraic Turbulence Models," *AIAA Journal*, Vol. 33, No. 10, 1995, pp. 1979–1981.

[7] Baldwin, B. S., and Lomax, H., "Thin Layer Approximation and Algebraic Model for Separated Turbulent Flows," AIAA Paper 78-257, 1978.

[8] Chakrabartty, S. K., "A Finite Volume Nodal Point Scheme for Solving Two Dimensional Navier-Stokes Equations," *Acta Mechanica*, Vol. 84, Nos. 1–4, March 1990, pp. 139–153.

[9] Jameson, A., Schmidt, W., and Turkel, E., "Numerical Solution of the Euler Equations by Finite Volume Methods Using Runge-Kutta Time Stepping Schemes," AIAA Paper 81-1259, 1981.

[10] Swanson, R. C., and Turkel, E., "A Multistage Time-Stepping Scheme for the Navier-Stokes Equations," AIAA Paper 85-0035, June 1985.

[11] Chakrabartty, S. K., and Dhanalakshmi, K., "Navier-Stokes Analysis of Korn Airfoil," *Acta Mechanica*, Vol. 118, Nos. 1–4, March 1996, pp. 235–239.

[12] Chakrabartty, S. K., Dhanalakshmi, K., and Mathur, J. S., "Navier-Stokes anlysis of flow through two-dimensional cascades," *Computational Fluid Dynamics Journal*, Vol. 10, No. 2, July 2001, pp. 233–241.

[13] Giguere, P., Lemay, J., and Dumas, G., "Gurney Flap Effects and Scaling for Low-Speed Airfoils," AIAA Paper 95-1881, June 1995.